Journal of Solid State Chemistry 187 (2012) 300–308

Contents lists available at SciVerse ScienceDirect

Journal of Solid State Chemistry

journal homepage: www.elsevier.com/locate/jssc

Study of surface fluorination of photocatalytic TiO_2 by thermal shock method

Tien Khoa Le [a,b], Delphine Flahaut [a,*], Dominique Foix [a], Sylvie Blanc [a], Huu Khanh Hung Nguyen [b], Thi Kieu Xuan Huynh [b], Hervé Martinez [a]

[a] IPREM/ECP (UMR 5254), University of Pau, Hélioparc, 2 av. Pierre Angot, 64053 Pau cedex 9, France
[b] University of Science – Ho Chi Minh city, 227 Nguyen Van Cu Street, Ho Chi Minh City, Vietnam

ARTICLE INFO

Article history:
Received 24 August 2011
Received in revised form
16 January 2012
Accepted 18 January 2012
Available online 28 January 2012

Keywords:
Fluorinated TiO_2
Structure characterization
XPS
Photocatalytic activity

ABSTRACT

Surface fluorinated TiO_2 powders were prepared by thermal shock method and an overall comparative study was achieved on the basis of XRD, SEM, UV–vis and XPS analyses. The main objective was to elucidate the influences of surface fluorination on the crystallite structures, morphologies, optical properties and surface chemistry with the temperature. According to the results, the surface fluorination under thermal shock method below 600 °C did not change the crystallite structure and the particles size, but successfully created chemisorbed fluoride ions, oxygen vacancies and increased the hydroxyl groups on the surface of TiO_2. The presence of oxygen vacancies was assigned to the red shift of TiO_2 optical absorption edge, which was the origin of visible-light-induced photocatalytic activity of these samples. For the thermal shock temperatures over 600 °C, the $K_2Ti_6O_{13}$-like phase was formed, resulting from the decrease of surface hydroxyl groups and the blue shift in absorption edge which reduced the photocatalytic activity.

1. Introduction

In recent years, photocatalytic technology based on TiO_2 has provided promising means for the treatment and the destruction of non-biodegradable organic pollutants in wastewater. Different from the other traditional methods like adsorption on active carbon, use of oxidants or biological methods, TiO_2 photocatalyst presents many advantages: it can operate at room temperature without oxidizing agents and can directly use solar energy or an artificial light source to initialize reactions [1]. Moreover, TiO_2 is chemically stable, cheap and environment-friendly. However, the activity of TiO_2 is not high enough for practical applications. This oxide mostly operates under UV irradiation, which occupies 3–5% of solar energy and its surface modification is a principal challenge in this research field to improve its photocatalytic activity [2,3].

It is well known that most of photocatalytic reactions occur on the catalyst surface and TiO_2 specificities such as the presence of surface hydroxyl groups, particles size distribution, surface defects, surface metal deposits, and adsorbates or surface complexes which have a direct influence on its photocatalytic activity. Some studies reported TiO_2 surface modifications by anions as SO_4^{2-} [4] or PO_4^{3-} [5] associated with their photocatalytic tests on degradation of organics pollutants in water such as trichloroethylene, acetaldehyde and toluene show a better activity for the modified photocatalyst in comparison with the non-modified TiO_2 [4].

Moreover, Minero et al. [6] have successfully increased the photocatalytic activity of TiO_2 by a surface fluorination process (in agreement with the general relation 1). In a first assumption, the presence of fluoride anions on the surface could be ascribed to the markedly enhanced photocatalytic oxidation of phenol [6]:

$$\equiv Ti{-}OH + F^- = \equiv Ti{-}F + OH^- \quad pKa_1 = 6.3 \qquad (1)$$

Same interests for the surface fluorination of TiO_2 powders and thin films have been reported [7–13]. For instance, the photocatalytic activity of fluorinated TiO_2 catalysts was then highly recommended for the degradation of many dyes, such as methylene blue, rhodamine B or reactive orange 4 [7–11]. However, these studies were mostly carried out under UV irradiation, and the more significant breakthrough toward visible light response by the surface fluorination has not been achieved. Recently, Junqi et al. [14] reported that the surface fluorination by solvothermally treatment could remarkably enhance the photocatalytic activity of TiO_2 hollow spheres in the case of the degradation of methyl orange under the visible light illumination. Some authors have attributed the enhanced visible-light-induced photocatalytic performance of fluorinated TiO_2 to a shift of absorption edge towards the longer wavelength in the band gap transition [15]. This reduced band gap leads to a more effective absorption of photons in the visible region, which produces more photogenerated electrons/holes, and therefore increases the photocatalytic activity of TiO_2. However, so far,

* Corresponding author. Fax: +33 5 59 40 76 22.
E-mail address: delphine.flahaut@univ-pau.fr (D. Flahaut).

0022-4596/$ - see front matter © 2012 Elsevier Inc. All rights reserved.
doi:10.1016/j.jssc.2012.01.034

the origin of this absorption shift due to surface fluorination has not been elucidated yet.

In this work, we describe a new and efficient approach for the preparation of fluorinated TiO_2 powders by thermal shock method and investigate the influence of surface fluorination on phase structure, particles size, optical absorption properties and surface properties. The X-ray photoelectron spectroscopy (XPS) is used to monitor the influence of fluorination on the TiO_2 surface as it provides both compositional and chemical state information of atoms and ions on the outer surface layers.

2. Experimental

2.1. Fluorination of TiO_2 P25

TiO_2 P25, a mixture of anatase and rutile with a primary particles size of 20–30 nm, purchased from Evonik Aeroxide, was used as the target catalyst to fluorinate because it is so far the best commercial photocatalyst. KF (99%, extra pure grade) was obtained from Sigma Aldrich and methylene blue (MB) (analytical grade) from Merck. TiF_4 (99%) was purchased from Acros Organics and used as a reference sample for XPS analysis. All chemicals were used in this study as received without further purification. Distilled water was used in all the experiments.

The photocatalyst TiO_2 P25 was suspended in 10 mL of a KF solution (0.625 mol L^{-1}) with the molar ratio of fluorine to titanium of 1:1 for 15 min under magnetic stirring. The obtained white suspension was filtered and dried at 150 °C for 3 h. The resulting powders were rapidly put into a furnace for thermal shock (TS) sequences of 5 min at several temperatures: 400, 500, 600, 700, 800 and 950 °C, respectively. After 5 min, the corresponding treated samples were directly removed from the furnace and cooled down in air to room temperature. Then, the samples were washed with 100 mL of distilled water and filtered out through a membrane for 5 times to remove the remained KF on the surface of samples and dried again at 150 °C for 1 h. In the following manuscript, all fluorinated samples were labeled as FTO-X (with X the temperature of thermal shock process). A sample without fluorination was also prepared by TS process at 500 °C, named P25-500, in order to elucidate the role of each of two processes, thermal shock and fluorination, in the activity of TiO_2.

2.2. Characterization

The powder X-ray diffraction (XRD) patterns obtained on a SIEMENS D5000 X-ray diffractometer using Cu $K\alpha$ radiation ($\lambda=1.5406$ Å) were used to investigate crystallite structures and phase compositions of samples. The acceleration voltage and the applied current were 40 kV and 25 mA, respectively.

The surface atomic composition and chemical environment were analyzed by X-ray photoelectron spectra (XPS) measurements on a Thermo K-alpha system with a hemispherical analyzer and a microfocussed (analysis area was ca. 200 μm^2) monochromatized radiation Al $K\alpha$ line (1486.6 eV) operating at 75 W under a residual pressure of 1×10^{-7} mbar. The XPS spectrometer was directly connected to a nitrogen dry gloves box in order to prevent the samples from moisture or air. For TiF_4, the XPS analysis was performed with a Kratos Axis Ultra spectrometer, using also a focused monochromatized Al $K\alpha$ radiation ($h\nu=1486.6$ eV). The pressure inside the analysis chamber was around 5×10^{-9} mbar. The temperature was regulated at −140 °C to avoid the possible degradation due to X-ray beam and the possible sublimation of TiF_4 under vacuum. The spectrometer pass energy was set to 200 eV (Thermo K-alpha) or 160 eV (Kratos Axis Ultra) for survey spectrum and to 20 eV for core peak records. Surface charging was minimized using a neutralizer gun, which sprays the low energy electrons and Ar^+ ions over the sample surface. All the binding energies were calibrated with the C1*s* peak at 285.0 eV originating from the surface contamination carbon. The treatment of core peaks was carried out using a nonlinear Shirley-type background [16]. A weighted least-squares fitting method using 70% Gaussian, 30% Lorentzian line shapes was applied to optimize the peak positions and areas. The quantification of surface composition was based on Scofield's relative sensitivity factors [17].

Crystallites size and shape were observed by a scanning electron microscopy (SEM) with Auger Microprobe JAMP 9500F operating at the probe current of 10^{-10} A and 30 keV and a working distance (source/sample) of about 20 mm.

The diffuse reflectance spectra of the powder sample were measured with a Perkin-Elmer Lamda 850 Spectrophotometer equipped with a 15 cm diameter integrating sphere bearing the holder in the bottom horizontal position. They were recorded at room temperature in steps of 1 nm, in the range 300–400 nm with a bandwidth of 2 nm. The instrument was calibrated with a certified Spectralon white standard (Labsphere, North Sutton, USA). The Kubelka–Munk model described light penetration in homogenous and optically thick media with only two parameters: an absorption coefficient, *K*, and an isotropic scattering coefficient, *S* (both have units of cm^{-1}) [18,19]. This model allowed us to deduce that there was a simple relationship (2) between the reflectance at "infinite thickness" and the absorption and scattering coefficients:

$$F(R_\infty)=(1-R_\infty)^2/(2-R_\infty)=K/S \quad (2)$$

3. Results and discussion

3.1. Phase structures

XRD was used to study the effects of fluorination on the crystallite structures and phase compositions of samples. Fig. 1 shows the XRD patterns of the bare and the fluorinated TiO_2 catalysts at different TS temperatures. The Rietveld refinement was carried out using the Fullprof 2009 structure refinement software [20]. The cell parameters and percentage of different crystallographic phases are summarized in Table 1. The TiO_2 P25 consists of a mixed phase of anatase (space group $I4_1/amd$, JCPDS No. 21-1272) and rutile (space group $P4_2/mnm$, JCPDS No. 21-1276) in the ratio of about 90:10. The anatase and rutile forms are identified with the XRD peaks at $2\theta=25.25°$ ((1 0 1) line) and $2\theta=27.42°$ ((1 1 0) line), respectively. No additional phase is detected for the fluorinated samples prepared up to 500 °C. Some studies [21,22] reported that the presence of fluoride ions on the surface of TiO_2 can enhance the crystallization of anatase phase and promote the growth of crystallites. However, for the FTO-500 sample, a slight decrease of anatase phase amount is observed (Table 1). The width of peaks in FTO-400 and FTO-500 spectra remains unchanged in comparison with P25 sample, indicating that our fluorination method at this TS temperature range do not modify the oxide crystallite size.

When the TS temperature exceeds 600 °C, an additional crystallographic phase, $K_2Ti_6O_{13}$ is observed (space group $C2/m$, JCPDS No. 73-1398). The arrangement of this crystalline structure corresponds to a 3D network of TiO_6 octahedra joined by corners and edges forming a zig-zag structure with rectangular tunnels along *y*-axis, in which potassium ions are located. The cell parameters of this new phase are comparable to those found by Dominko et al. [23]. XRD peak intensities of $K_2Ti_6O_{13}$ steadily become stronger while those of anatase and rutile were reduced

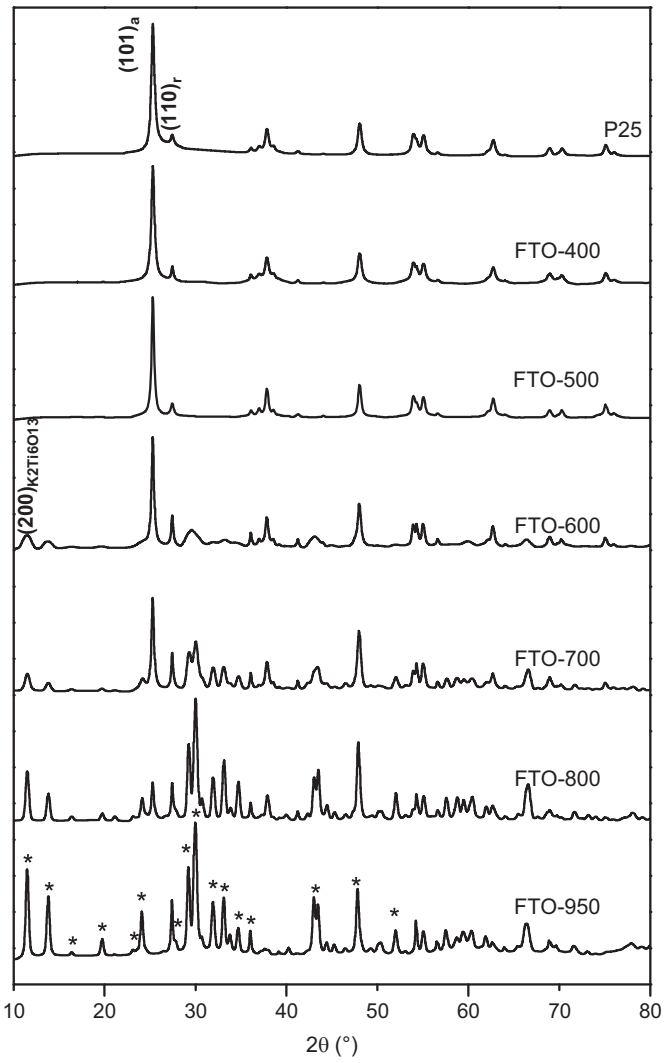

Fig. 1. XRD patterns of TiO_2 P25 and fluorinated samples (*a*, *r* and ∗ represent the anatase, rutile and $K_2Ti_6O_{13}$-type phases, respectively)

with the increase of the temperature (Fig. 1). It is to be noted that the anatase crystallographic form changes into rutile at ca. 600 °C. At 950 °C, almost both anatase and rutile phases are totally transformed into $K_2Ti_6O_{13}$.

In our case, the fluorination is performed by the reaction in solution of the KF and TiO_2 precursors. However, they are also used by several authors as precursors of the synthesis of the $K_2Ti_6O_{13}$ crystalline phase at around 700 °C [24,25]. This clearly explains the appearance of this phase in our fluorination conditions at TS temperature of 600 °C.

3.2. Morphology of the photocatalysts

The morphologies and microstructure of the samples were further investigated by SEM. The SEM micrograph (180,000 × magnification) of TiO_2 P25 sample includes sphere-like particles, presented in an agglomerated status with a homogeneous size distribution of 20–50 nm (Fig. 2a). The size and shape of particles remained unchanged despite the fluorination by TS up to 500 °C (Fig. 2b).

In addition, the crystallite diameter was also calculated from the full width of half maximum (FWHM) of diffraction peaks by using the Debye–Scherrer formula (3). The most intense diffraction lines for anatase (1 0 1) and rutile (1 1 0) were, respectively, selected to calculate the average size of each crystallite phases using

$$D_{hkl} = \frac{k\lambda}{\beta \cos\theta} \tag{3}$$

where D_{hkl} is the crystallite size, k is the constant dependent on crystallite shape (0.9), λ is the wavelength of copper $K\alpha$ X-ray radiation (1.5405 Å) , β is the FWHM of the most intense peak and θ is the diffraction angle. The crystallite size is found to be in nanoscale and about 20–35 nm for both anatase and rutile phase in our samples (Table 2), which is consistent to the particle sizes estimated from SEM micrographs.

Nevertheless, for the TS temperature above 600 °C, the SEM micrograph (18,000 × magnification) indicates the apparition of small rod-like among TiO_2 spherical particles, according to the formation of the anisotropic $K_2Ti_6O_{13}$ phase detected by the XRD

Table 1
Phase composition and Unit cell parameters of TiO_2 P25 and fluorinated samples.

Samples	Anatase		Rutile		$K_2Ti_6O_{13}$	
	Fraction (%) (R_{Bragg}/R_f)	Unit cell parameters	Fraction (%) (R_{Bragg}/R_f)	Unit cell parameters	Fraction (%) (R_{Bragg}/R_f)	Unit cell parameters
TiO_2 P25	89.8 ± 0.8 (13.6/20.5)	$a=b=3.7864(2)$ Å $c=9.5049(8)$ Å	10.1 ± 0.3 (55.1/48.1)	$a=b=4.595(1)$ Å $c=2.959(2)$ Å		
FT1-400	90.0 ± 0.9 (12.6/11.3)	$a=b=3.7869(5)$ Å $c=9.506(2)$ Å	10.0 ± 0.5 (34.7/30.9)	$a=b=4.593(1)$ Å $c=2.959(2)$ Å		
FTO-500	86 ± 2 (19.9/12.0)	$a=b=3.7875(6)$ Å $c=9.506(2)$ Å	13.9 ± 0.6 (30.8/18.8)	$a=b=4.595(2)$ Å $c=2.958(2)$ Å		
FTO-600	63 ± 2 (24.0/12.7)	$a=b=3.7895(7)$ Å $c=9.508(2)$ Å	18.7 ± 0.7 (21.2/14.2)	$a=b=4.595(2)$ Å $c=2.960(2)$ Å	18.1 ± 0.7 (41.3/31.4)	$a=15.65(2)$ Å $b=3.794(2)$ Å $c=9.161(7)$ Å $\beta=99.94(5)°$
FTO-700	34.3 ± 0.9 (16.9/11.2)	$a=b=3.7878(9)$ Å $c=9.503(3)$ Å	17.1 ± 0.6 (13.0/10.2)	$a=b=4.592(2)$ Å $c=2.959(2)$ Å	48.5 ± 0.5 (20.3/17.0)	$a=15.593(5)$ Å $b=3.7962(9)$ Å $c=9.122(3)$ Å $\beta=99.77(3)°$
FTO-800	13.3 ± 0.7 (14.3/12.6)	$a=b=3.790(2)$ Å $c=9.510(7)$ Å	15.3 ± 0.7 (17.1/9.71)	$a=b=4.596(2)$ Å $c=2.962(2)$ Å	71 ± 2 (21.6/16.9)	$a=15.608(4)$ Å $b=3.7980(7)$ Å $c=9.119(2)$ Å $\beta=99.77(2)°$
FTO-950			6.1 ± 0.2 (8.81/8.52)	$a=b=4.6014(6)$ Å $c=2.9650(7)$ Å	93.8 ± 0.8 (15.3/11.2)	$a=15.621(3)$ Å $b=3.8039(4)$ Å $c=9.1255(9)$ Å $\beta=99.758(8)°$

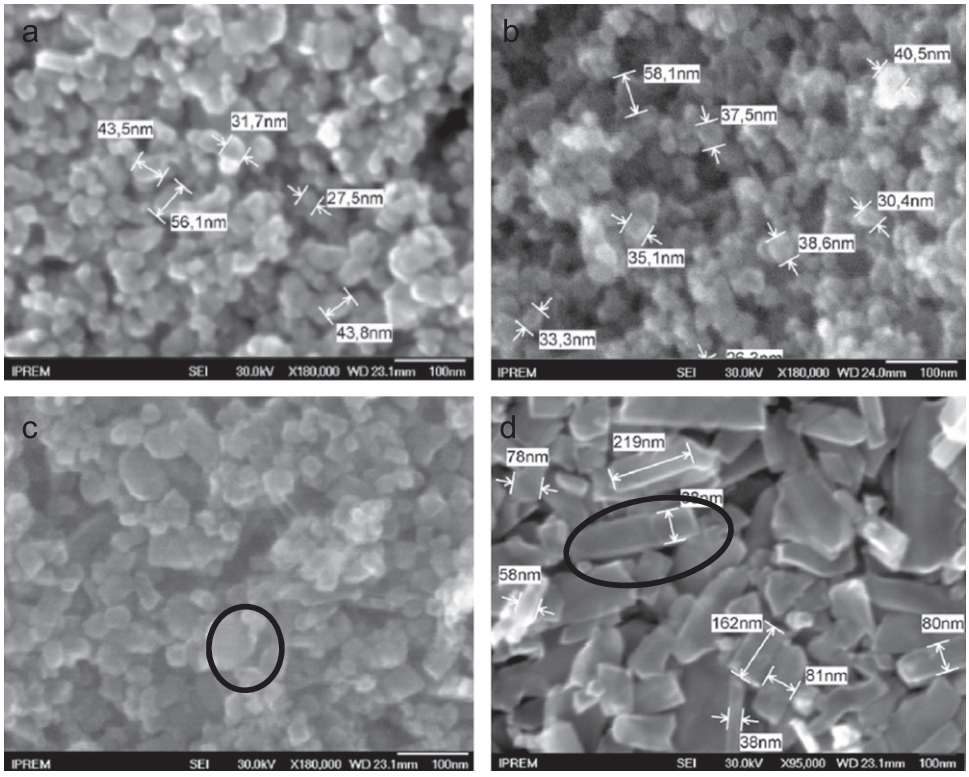

Fig. 2. SEM micrographs of (a) TiO_2 P25, (b) FTO-500, (c) FTO-600 and (d) FTO-950.

Table 2
Crystallite size (for anatase, rutile) and band gap value calculated from XRD patterns and UV–vis diffuse reflectance spectra, respectively.

Sample	Anatase % (crystallite size (nm))	Rutile % (crystallite size (nm))	$K_2Ti_6O_{13}$	Eg (eV)	
				$(F(R)hv)^{1/2}$, $\gamma=2$ Indirect allowed	$(F(R)hv)^2$, $\gamma=0.5$ Direct allowed
FTO-950	–	6.1 (34.1)	93.8	3.67	3.68
FTO-800	13.3 (31.4)	15.5 (34.2)	71	3.24	3.65
FTO-700	34.3 (26.4)	17.1 (36.3)	48.5	3.15	3.61
FTO-600	63.0 (23.9)	18.7 (32.5)	18.1	3.09	3.56
FTO-500	86.0 (20.7)	13.9 (29.5)	–	2.95	3.55
FTO-400	90.0 (17.7)	10.0 (22.2)	–	2.85	3.49
P25	89.8 (21.6)	10.1 (26.9)	–	3.21	3.64

patterns. The mixed morphology clearly shows a phase transition from TiO_2 to $K_2Ti_6O_{13}$ from the TS temperature of 600 °C (Fig. 2c). Moreover, we observed an increase of the length and the amount of $K_2Ti_6O_{13}$ particles with the TS temperature. Fig. 2d put in evidence that these rod-like particles could reached about 500–1000 nm in length in the FTO sample prepared at 950 °C.

3.3. XPS analysis

The surface fluorination and the relative concentration and chemical environment of F, O, Ti and C atoms on the surface of the catalysts were followed by XPS. The results are reported in Table 3. The C1*s* core peaks due to surface contamination carbon are deconvoluted into three peaks: the main peak at 285.0 eV associated with C–C or C–H bonds, the peak at 286.6 eV with C–O bonds and the peak at 289.4 eV with O=C–O bonds. Figs. 3 and 4 present, respectively, the Ti2*p* and F1*s* core peaks of the bare TiO_2 P25 and fluorinated samples at different TS temperatures. Due to spin–orbit coupling, each spectrum exhibits two main Ti2*p* components located at 459.1 (Ti2$p_{3/2}$) eV and 464.9 eV (Ti2$p_{1/2}$). These binding energies (B.E) are representative of the tetravalent Ti^{4+} in an oxygen environment of titanium, which is coherent with the XPS data for TiO_2 analyzed in our laboratory [26–28] and to the literature [29,30]. In addition, the spectra also contain distinct charge-transfer satellite peaks at 13 eV above the 2$p_{3/2}$ and 2$p_{1/2}$ peaks positions. The origin of Ti2*p* satellite peaks is under debate [31–35] and one of the explanations can be the strong covalency hybridization between the metal *d* and the oxygen *p* orbitals [31]. The main peaks are mainly characterized by the well screened final state configuration $2p^5 3d^1 L^{-1}$ where *L* denotes the ligand electron [32]. The satellite peaks are caused by the hole–particle pair "shake-up" excitation on the anions in the presence of the ligand-metal charge transfer screened core hole. They mostly correspond to the final state configurations $2p^5 d^0$ and $2p^5 d^1 L^{-1} L'L''^{-1}$ [35]. The fluorination does not affect the Ti2*p* core peaks for all samples certainly due to the low coverage of the surface by fluoride ions.

XPS analysis of TiF_4 as reference sample was carried out in order to elucidate the chemical environment of fluorine species in our catalysts. The F1*s* core peak of this compound is located at 684.8 eV. For all fluorinated samples, the XPS F1*s* spectra present a peak at about 684.7–685.1 eV. This peak could be attributed to the fluoride ions chemisorbed on the surface (F_I) [7,14,36] or fluoride ions of TiF_4 from our reference. However, in TiF_4, the Ti2$p_{3/2}$ and Ti2$p_{1/2}$ components are, respectively, found at 461.6 and 467.3 eV. The shift toward high B.E of these components is due to the fluoride environment, compared to oxygen environment in TiO_2. This result implies that the fluorine species observed on the surface of fluorinated samples correspond only to chemisorbed fluoride ions. The B.E difference ΔE_B (Ti2$p_{3/2}$–F1*s*) was determined in order to estimate the electronic density between the Ti element and F element on the surface with a

Table 3
High resolution XPS data of TiO_2 P25 and fluorinated samples.

	P25		FTO-400		FTO-500		FTO-600		FTO-700		FTO-800		FTO-950	
	B.E. (FWHM) eV	%	B.E (eV)	%	B.E (eV)	%	B.E (eV)	%	B.E (eV)	%	B.E (eV)	%	B.E (eV)	%
C1*s*	285.0 (1.6)	5.6	285.0 (1.6)	4.5	285.0 (1.5)	9.8	285.0 (1.5)	9.2	285.0 (1.5)	12.4	285.0 (1.5)	10.7	285.0 (1.5)	10.2
	286.7 (1.6)	1.2	286.6 (1.5)	0.7	286.7 (1.6)	1.6	286.6 (1.5)	1.7	286.6 (1.3)	1.9	286.5 (1.3)	1.4	286.6 (1.1)	0.6
	289.4 (1.5)	0.8	289.4 (1.5)	0.6	289.4 (1.6)	0.8								
Ti2$p_{3/2-1/2}$	459.1–464.9 (1.0–1.9)	28.8	459.1–464.8 (1.1–1.9)	28.9	459.1–464.8 (1.0–1.9)	26.1	459.1–464.9 (1.1–2.0)	25.1	459.1–464.8 (1.1–2.0)	23.8	459.1–464.9 (1.1–2.0)	23.8	459.1–464.8 (1.2–2.1)	22.9
Satellites	472.3–478.2		472.2–478.4		472.2–478.4		472.2–478.4		472.1–478.3		472.1–478.3		472.0–478.2	
O1*s* I	530.4 (1.1)	57.8	530.4 (1.2)	53.9	530.3 (1.1)	48.8	530.5 (1.2)	46.8	530.5 (1.2)	45.9	530.6 (1.2)	47.3	530.6 (1.3)	45.5
O1*s* II	531.6 (1.5)	5.9	531.6 (1.6)	6.5	531.5 (1.6)	8.2	531.5 (1.6)	6.5	531.7 (1.6)	6.1	531.8 (1.6)	5.1	531.8 (1.7)	4.8
F1*s* I			684.7 (1.7)	3.0	684.7 (1.7)	3.4	684.9 (1.6)	5.2	684.9 (1.6)	3.8	685.0 (1.6)	3.7	685.1 (1.7)	5.8
F1*s* II											687.0 (1.7)	0.2	686.9 (1.8)	0.6
K2$p_{3/2-1/2}$ I			293.0–295.7 (1.1–1.2)	0.6	293.1–296.0 (1.1–1.0)	0.7	292.8–295.6 (1.1–1.1)	3.7	292.7–295.5 (1.0–1.0)	4.2	292.8–295.5 (1.0–1.0)	6.2	292.8–295.5 (1.1–1.1)	7.9
K2$p_{3/2-1/2}$ II			293.9–296.7 (1.4–1.4)	1.1	294.1–297.1 (1.3–1.4)	0.5	293.7–296.4 (1.3–1.4)	1.7	293.5–296.1 (1.4–1.4)	1.7	293.8–296.4 (1.3–1.3)	1.5	293.9–296.6 (1.2–1.2)	1.7
ΔE_B (Ti2*p*-O1*s*) (eV)	71.3		71.3		71.2		71.2		71.4		71.5		71.5	
O_I/Ti	2.00		1.86		1.87		1.86		1.93		1.98		1.99	
O_{II}/Ti	0.20		0.23		0.31		0.26		0.26		0.21		0.21	
ΔE_B (Ti2*p*-F1*s*) (eV)			225.6		225.6		225.8		225.8		225.9		226.0	
F_I/Ti			0.10		0.13		0.21		0.16		0.16		0.25	

more or less ionic (or covalent) character (Table 3). If the F1*s* peak shifts toward the higher B.E (F^- less negative) and Ti2$p_{3/2}$ main component shifts to the lower B.E (Ti^{4+} less positive), the direct interaction between these ions gets more covalent, corresponding to the increase of ΔE_B (Ti2$p_{3/2}$–F1*s*) values. Along the TS treatment, it was observed that ΔE_B (Ti2$p_{3/2}$–F1*s*) values slightly increase for the samples fluorinated from 400 to 950 °C, which brings out the fact that the Ti–F bond becomes more covalent with TS temperature. However, above the TS temperature of 800 °C, an additional weak component appears at higher B.E, about 687.0 eV (F_{II}). This component was attributed to fluorine atoms in oxygenated environment of solid solution $TiO_{2-x}F_x$, which is originated from the substitution of F ions for O ions in the TiO_2 lattice [36–38] as the ionic radii value of F^- anion (~1.3 Å) is similar to that of O^{2-} anion (~1.4 Å) [39]. The F1*s* core peak evolution indicates that the fluorination at TS temperatures below 800 °C only took place on the surface of catalyst but from 800 °C, the fluorine atoms were inserted in the TiO_2 lattice. We put in evidence an increase of the fluorine content on the surface with a slight insertion in the bulk TiO_2 for the TS temperature of 800–950 °C (Table 3).

The O1*s* XPS spectra (not shown in this paper for a non-exhaustive presentation) of all samples present rather the same characteristics (Table 3). The O1*s* core peaks of TiO_2 P25 and FTO samples consist of a main peak located at 530.4 eV (O_I) assigned to oxygen atoms of the oxide lattice and a minor peak at 531.6 eV (O_{II}) assigned to surface OH species [27]. The calculation of O_{II}/Ti area ratio indicates highest values for fluorinated catalysts compared to bare TiO_2 P25 sample (Table 3). The maximum reached to 0.31 in the FTO-500 sample. This suggests that an increase of surface's hydroxyl group amount can be reached by the surface fluorination of catalysts. Moreover, the O_I/Ti atomic ratio of fluorinated samples prepared from 400 to 600 °C was found to be lower than 2, the stoichiometric O_I/Ti atomic ratio of TiO_2 (Table 3). The substoichiometry indicates that the fluorination by TS method in this temperature range probably formed the oxygen vacancies on the surface.

The K2*p* core peaks (not shown) were also detected in the fluorinated samples. The fitting analysis of the K2*p* spectra reveals two different environments for potassium. Due to spin–orbit coupling, the first one (K_I) shows the K2$p_{3/2}$ peak located around 293.0 eV and the K2$p_{1/2}$ around 295.7 eV, corresponding to the oxidized potassium associated with lattice oxygens [40]. The second one (K_{II}) has two main components located at higher B.E, around 293.9 eV (K2$p_{3/2}$) and 296.7 eV (K2$p_{1/2}$). These energies, however, are lower than the B.E values of K2*p* main components in metallic potassium (K2$p_{3/2}$ 294.6 eV and K2$p_{1/2}$ 297.4 eV [41]). This suggests that the second K form corresponds to the positively charged K ion in titanium environment. The percentage of K species increased with the TS temperature in the samples fluorinated from 600 to 950 °C, which is consistent with the increase of $K_2Ti_6O_{13}$ concentration (Table 3). However, the presence of K2*p* peaks in the fluorinated samples without the formation of $K_2Ti_6O_{13}$ indicates that the fluorination by TS also produces potassium species on the surface of samples.

3.4. Optical properties

The optical responses of the of the bare and fluorinated TiO_2 P25 samples were analyzed using UV–visible diffuse reflectance and are shown in Fig. 5a. The band gap energy Eg can be evaluated by the Tauc plot (Fig. 5b), i.e., a plot of $(\alpha h\nu)^{1/\gamma}$ as a function of photon energy $h\nu$ [42]. This method assumes that the absorption product $\alpha h\nu$ is given by

$$\alpha h\nu = \alpha_0(h\nu - Eg)^{\gamma} \quad (4)$$

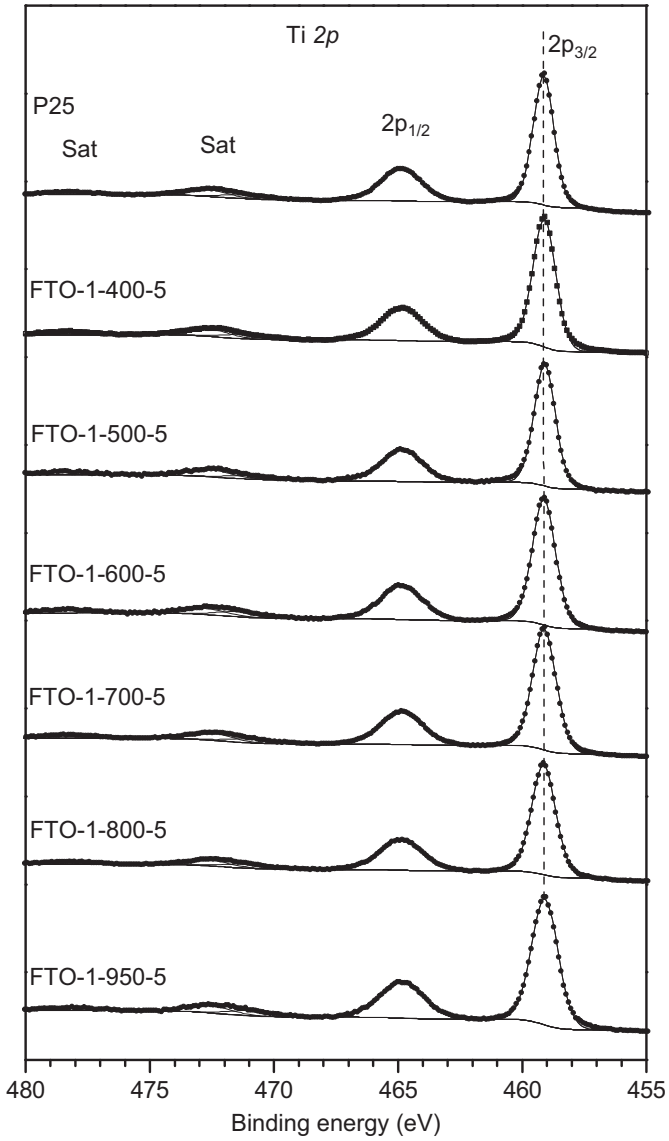

Fig. 3. Ti2*p* spectra of TiO_2 P25 and fluorinated samples.

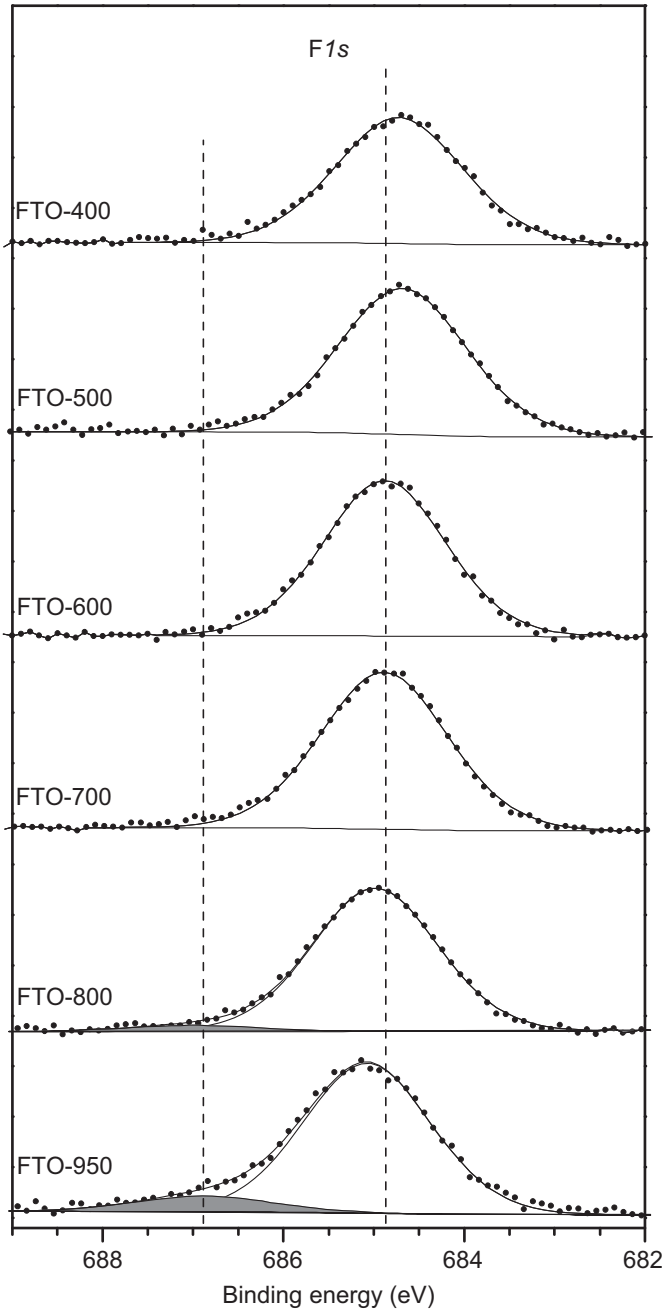

Fig. 4. F1*s* spectra of fluorinated samples. The filled peaks are assigned to the fluorine species in the oxygenated environment.

where α_0 is a material constant, the power coefficient γ can be: 1/2, 3/2, 2 or 3 depending on the type of the considered transition: direct allowed, direct forbidden, indirect allowed or indirect forbidden, respectively [43]. Eq. (4) is only valid over the strong absorption region and was originally used for the amorphous semiconductors [44]. The Kubelka–Munk function was applied for thick samples to convert diffuse reflectance measurements into the equivalent absorption coefficient. If the weak dependence of the scattering coefficient S on the wavelength is taken into account, K/S can be assumed then as proportional to the absorption within the narrow range, which is containing the fundamental absorption edge ($\alpha = K/S$).

One should note that semiconductors are classified as materials only with direct ($\gamma = 0.5$) or indirect ($\gamma = 2$) allowed transition. For nanoscale semiconductors most authors assume indirect transition for the calculation of the band gap and the Tauc plot is subsequently applied as $(\alpha h\nu)^{1/2}$ vs. $h\nu$. Eg is then estimated from the intercept with the x-axis ($\alpha = 0$) of the straight line fitted from the linear region.

Tang et al. [45] discussed the optical properties in rutile and anatase. Rutile has a band gap with transition close to indirect allowed case. Both experimental results and theoretical calculations suggest that TiO_2, rutile has a direct forbidden gap (3.03 eV), which is almost degenerate with an indirect allowed transition (3.05 eV) [46]. Due to the weak strength of the direct forbidden transition, the indirect allowed transition dominates in the optical absorption just above the absorption edge. The observed indirect allowed band gaps ($(F(R)h\nu)^2$, $\gamma = 0.5$) for our samples did not show significant variations ($\sim$3.6 eV) and did correspond to the rutile which is equal to 3.03 eV. The P25 and FTO-400 had similar structure but different direct allowed Eg value.

It was found that the fluorination by TS method obviously affects light absorption characteristics of TiO_2. TiO_2 P25 powder presents a direct allowed band gap of 3.21 eV. The absorption spectra of FTO samples prepared from 400 to 600 °C showed a red shift in the band gap transition, corresponding to a narrow band gap of 2.85–3.09 eV, respectively. Conversely, for the FTO powders prepared above

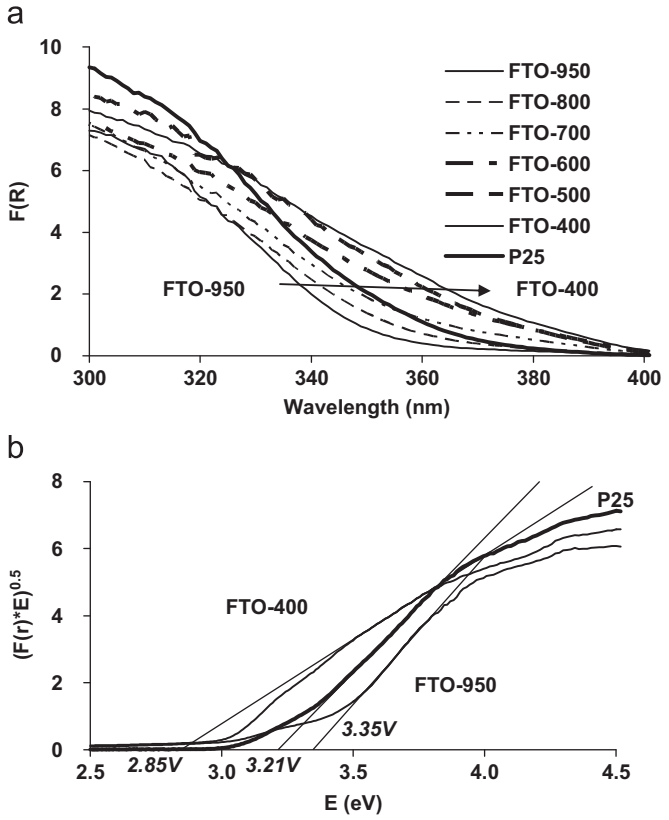

Fig. 5. (a) UV–visible diffuse reflectance spectra of TiO_2 P25 and fluorinated samples; (b) $(F(R)hv)^{0.5}$ vs. hv for FTO-400, FTO-950 and P25 (derived from previous figure), showing a linear relation between $(F(R)hv)^{0.5}$ and hv in the wavelength region of fundamental absorption edge.

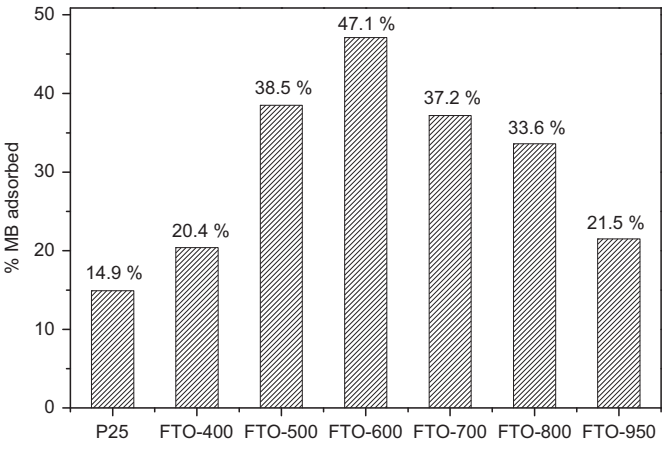

Fig. 6. Comparison of MB amount adsorbed on the surface of samples.

600 °C, a blue shift was detected. With the increase of TS temperature (> 600 °C), the width of band gap for the fluorinated samples increases from 3.09 eV to 3.67 eV.

3.5. Photocatalytic activity

Visible-light-driven photocatalytic performances of the bare and fluorinated TiO_2 P25 powders were tested in the degradation of methylene blue (MB). The use of methylene blue for photocatalyst tests is still widely reported in the literature [47]. Prior to the photocatalytic experiments, the MB adsorption on the surface of catalysts was determined stirring the MB solution with catalysts in the dark condition until the adsorption/desorption equilibrium

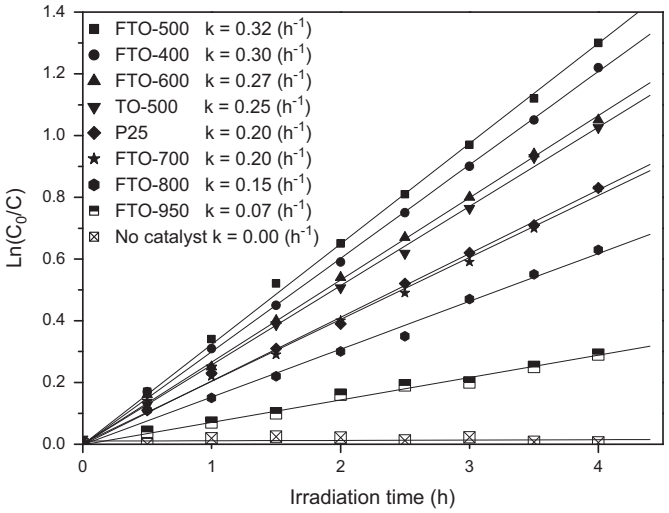

Fig. 7. $\mathrm{Ln}(C_0/C)$ versus time plot for determination of rate constants k (h^{-1}) of MB degradation under visible irradiation.

between the TiO_2 surface and the MB was established. Fig. 6 shows a comparison of adsorbed MB percentage onto different samples at the adsorption equilibrium. All fluorinated samples exhibit higher MB content on their surface than this obtained for the bare sample (14.9% of adsorbed MB). This can be explained by the fact that the adsorption process on the TiO_2 surface is driven by electrostatic interactions between organic molecules (BM) and the oxide surface. The existence of strongly electronegative fluoride ions on the surface of fluorinated samples may induce a negative charge on the surface sample and then promoted the adsorption of organic cationic compound such as MB. Thus, the FTO-600 sample, which contains the most important amount of F, showed the highest MB adsorption (47.1%) on its surface. Above TS temperature of 600 °C, the MB adsorption decreased dramatically according to the growth of catalyst particles. After the adsorption equilibrium was obtained, the MB degradation under visible light irradiation was carried out.

Fig. 7 compares the $\mathrm{Ln}(C_0/C)$ curves of MB degradation on different samples under visible light illumination. The net decomposition of MB in our system followed the pseudo-first-order Langmuir–Hinshelwood kinetic model. This is consistent with the previous works on MB degradation induced by photocatalysts [48,49]. The bare TiO_2 P25 sample exhibits the rate constant (k) of MB degradation of 0.20 h^{-1}. The FTO-400 and FTO-500 samples showed the best photocatalytic activities, with a rate constant of 0.30 and 0.32 h^{-1}, respectively. The rate constant of MB degradation decreases when the FTO samples were prepared from 600 to 950 °C, to reach 0.07 h^{-1} for FTO-950 sample. This indicated that the activity of fluorinated samples plays a role in the MB degradation. Since the TS temperature of 500 °C seems to be the best temperature for the enhancement of TiO_2 photocatalytic activity under visible light, the photocatalytic test on P25-500 was also performed to better understand the influence of the individual TS process. The rate constant of MB decomposition on P25-500 was 0.25 h^{-1}, indicating that the TS process can also increase the visible light induced performance of TiO_2. However, its activity is still inferior to that of FTO-500 ($k = 0.32\ h^{-1}$).

Next to the impact of the fluorination on the TiO_2 property, others mechanisms are involved in the MB degradation under visible light. First, some studies [50,51] reported that a weak degradation of MB can occur without photocatalyst under the visible light irradiation $\lambda > 420$ nm due to the photobleaching of MB observed in an oxygen-saturated aqueous solution [47]. Prior to the photocatalytic experiment, the MB photosensitization in absence of any photocatalyst was tested under the 420 nm lamp and no

degradation has been observed (Fig. 7), as already reported by Li et al. [52]. The use of this lamp and our experimental condition allow us to overcome the photobleaching of MB by the reaction with the oxygen singlet. Otherwise, the dye molecule can be excited under visible light and transfer an electron, which can be injected into the TiO_2 conduction band. Thereby, the MB can be degraded by photosensitization of TiO_2 samples. However, in the same experimental conditions, the reaction rate notably increases for the fluorinated samples. This indicated that beside the TiO_2-sensitized photobleaching of MB, the activity of fluorinated samples plays a role in the MB degradation. Thus, the surface fluorination by thermal shock method up to TS temperature of 500 °C is proved effective for the visible light responses of TiO_2 photocatalysts while considering the role of the MB photosensitization.

Beside the role of the photosensitization of the MB, this proves that the fluorination has mutual effects with the TS process to increase the photocatalytic activity of TiO_2.

4. Discussion

In our work, the TS method was used to fluorinate TiO_2 P25 in the wide temperature range from 400 to 950 °C. Although this method is very simple and easy to carry out, in our knowledge, there is no work until now studying the influences of the short-time heat treatment with KF on the bulk structure, surface chemistry, absorption properties and photocatalytic activities of TiO_2. These influences are expected to be very interesting since the instant heating and cooling of samples by TS process seem to be able to create strong bonds between fluorine and the TiO_2 surface without any modification of its structure and particle size. The XRD patterns indicate that the bulk structure of TiO_2 P25, containing two crystalline phases anatase and rutile, was not changed under the fluorination process up to 500 °C. For the fluorinated samples with TS < 500 °C, the SEM micrographs also show no modification in particle size and shape. Thus, the presence of F1*s* peak corresponding to fluoride species chemisorbed on the surface of FTO-400 and FTO-500 demonstrates that our TS method successfully fluorinated the surface of TiO_2 and this fluorination process did not affect neither crystallite structure nor morphology of TiO_2 P25 in the considered TS temperature range.

However, for the fluorinated samples prepared at TS temperatures from 600 °C to 950 °C, the XRD results exhibit a decrease of anatase amount and an increase of rutile amount in the bulk structure, which is consistent with a report of Nair et al. [53]. They investigated the influence of thermal treatment on phase composition of TiO_2 and found that from 650 °C, the anatase phase begins to transform into rutile phase. The XRD patterns also denoted the formation of $K_2Ti_6O_{13}$ phase which was also observed in the SEM micrographs, with the increase of particle size in these samples, meaning that our TS method used in this work will change the structure and the morphology of TiO_2 at high temperatures associated indeed to the formation of the $K_2Ti_6O_{13}$ phase. Moreover, the apparition of F1*s* peak attributed to F atoms in the solid solution $TiO_{2-x}F_x$ when the TS temperature exceeds 800 °C indicates that this method is also an easy way to insert the fluorine atoms into the oxygen sites of the TiO_2 crystal lattice.

In order to tune the electronic structure and extend the spectral respond of TiO_2 to visible light, titania could be doped with various elements such as N [54], S [55], co-doped with N–S [56] or Ag–AgCl [57]. Nonetheless, most of the studies reported that the surface fluorination does not cause any significant shift in the fundamental absorption edge [9,12]. Even the F-doping in the structure of TiO_2 does not change its optical properties [58,59]. These results were explained by theoretical band calculations [54,60], which indicate that the high density levels of F2*p* state are located below the valence band of TiO_2 and do not mix with any valence band or conduction band of TiO_2. Therefore, it is not expected that the presence of fluoride ions on the surface or in the TiO_2 lattice could narrow the band gap or create a new absorption band.

There are some reports [38,61,62] that the insertion of fluorine atoms into the oxygen sites can form two kinds of oxygen vacancies, F center with two trapped electrons and F^+ center with one trapped electron, in the bulk of TiO_2. These oxygen vacancies have the energy states located between valence and conduction bands, therefore they result in the band gap narrowing and then promote the visible-light-response photocatalytic activity. However, as far as we know, there are no reports on the creation of oxygen vacancy and band gap narrowing due to surface fluorination. Surprisingly, the UV–visible reflectance spectra of our samples clearly exhibit a red shift in the absorption edge, corresponding to a decrease of band gap from 3.21 eV for TiO_2 P25 to 2.85 and 2.95 eV for the catalysts fluorinated at 400 and 500 °C, respectively. This evolution may be explained by the changes of catalyst surface due to the fluorination in this TS temperature range, as no modification in structure and particles size was observed for FTO-400 and FTO-500. As mentioned in Section 3.3, the XPS spectra of the samples fluorinated from 400 to 600 °C showed the substoichiometric O_l/Ti ratio of about 1.86 on the surface (Table 3), which confirmed the formation of oxygen vacancies. Besides, the unique F1*s* peak attributed to chemisorbed F^- species in XPS spectra of these samples denotes that the oxygen vacancies were not formed via the F doping, but through the surface fluorination of TiO_2. These oxygen vacancies should be responsible to the red shift with a reduction of band gap and the enhanced visible light response. The increased photocatalytic activity for MB degradation under visible light was found in FTO-400 ($k = 0.30\ h^{-1}$) and FTO-500 ($k = 0.32\ h^{-1}$) samples, corresponding, respectively, to a band gap value of 2.85 and 2.95 eV. Hence, the surface fluorination by TS method is proved to be a new approach to create the visible light induced activity of TiO_2. Nonetheless, the contribution of the photobleaching and the photosensitization of the TiO_2 under visible light have also to be taken into account. The facility to carry out of this method also makes it become a promising means, which can be widely applied to improve TiO_2 photocatalyst.

When the FTO samples were prepared at TS temperatures above 600 °C, the UV–visible reflectance spectra showed a blue shift in absorption edge, corresponding to the decrease of oxygen vacancies amount. According to some theories [63,64] the observed blue shift of the fundamental absorption edge of TiO_2 can be related to the decrease in the average crystallite size, which can cause a shift of the Eg of about 0.2 eV to higher energies, due to so-called quantum size effect. But for these samples, we did not observe such effect as the particle size increases with the TS temperatures. Thus, the increase of band gap values would be ascribed to the decrease of anatase amount and the formation of a titanate phase, $K_2Ti_6O_{13}$ which were monitored by XRD and SEM experiments. The absorption properties of titanate phases $M_2Ti_6O_{13}$ (M = Na, K) and their photocatalytic activity for the degradation of water pollutants have been also studied [65–70]. Both $K_2Ti_6O_{13}$ and $Na_2Ti_6O_{13}$ show the band gap values of 3.4–3.5 eV [70], higher than the band gap value obtained in our work for TiO_2 P25 (3.21 eV). Thus, the titanate phases can only play as effective photocatalysts under UV light irradiation. This explains the blue shift and the decrease of visible-light-induced photocatalytic activity when the $K_2Ti_6O_{13}$ amount becomes considerable in our catalysts with the high TS temperatures. The FTO-950 sample whose the structure mainly contains $K_2Ti_6O_{13}$ phase presents the highest band gap value (3.67 eV), and so the lowest rate constant of MB degradation under visible light ($k = 0.07\ h^{-1}$). All these results indicate that the surface fluorination using TS can play a role as one of new methods of TiO_2 modification, which allow to modify its band gap and then its

photocatalytic activity. Besides, the enhanced photocatalytic performance of P25-500-5 also suggested that the individual TS method has its own effects on TiO_2 activity. Thus, the influences of the individual TS process on the bulk structure, surface properties, morphology and optical absorption properties as well as photocatalytic activity of TiO_2 should be further investigated in the next studies.

5. Conclusion

In this study, the TiO_2 P25 powders were fluorinated by thermal shock methods at different temperatures. The results of XRD, SEM, XPS analysis clearly indicated that this method performed at temperatures below 600 °C allows one to keep unchanged the crystallite structure, the morphology and successfully fluorinates the surface of TiO_2. The surface fluoride amount and the surface O_{II}/Ti atomic ratio increase with the TS temperatures from 400 to 600 °C. Surface fluorination also creates some oxygen vacancies, which generate the visible-light-induced photocatalytic activity. The optimum samples were FTO-400 and FTO-500 which showed the strongly higher photocatalytic activity than commercial TiO_2 P25 under visible light irradiation. Since 600 °C, the fluorination by TS begins to form the $K_2Ti_6O_{13}$ phase. The increase of $K_2Ti_6O_{13}$ phase content with TS temperatures from 600 to 950 °C was attributed to the increase of band gap value and the decrease of photocatalytic activity. In conclusion, the surface fluorination of TiO_2 by TS method without structure and particles size modification was demonstrated to be one of simple methods, which permits to prepare some photocatalysts more active than TiO_2 P25 in wavelength visible zone.

References

[1] A. Fujishima, T.N. Rao, D.A. Tryk, J. Photochem. Photobiol. C 1 (2000) 1.
[2] M. Anpo, Bull. Chem. Soc. Jpn. 77 (2004) 1427.
[3] A.L. Linsebigler, G. Lu, J.T. Yates, Chem. Rev. 95 (1995) 735.
[4] D.S. Muggli, L. Ding, Appl. Catal. B: Environ. 32 (2001) 181.
[5] J.C. Yu, L.Z. Zhang, Z. Zheng, J.C. Zhao, Chem. Mater. 15 (2003) 2280.
[6] C. Minero, G. Mariella, V. Maurino, E. Pelizzetti, Langmuir 16 (2000) 8964.
[7] S.Y. Yang, Y.Y. Chen, J.G. Zheng, Y.J. Cui, J. Environ. Sci. 19 (2007) 86.
[8] J. Tang, H. Quan, J. Ye, Chem. Mater. 19 (2007) 116.
[9] Y. Chen, F. Chen, J. Zhang, Appl. Surf. Sci. 255 (2009) 6290.
[10] A. Vijayabalan, K. Selvam, R. Velmurugan, M. Swaminathan, J. Hazard. Mater. 172 (2009) 914.
[11] Q. Xiang, J. Yu, Mietek Jaroniec, Chem. Commun. 47 (2011) 4532.
[12] H. Park, W. Choi, J. Phys. Chem. B 108 (2004) 4086.
[13] J.S. Park, W. Choi, Langmuir 20 (2004) 11523.
[14] L. Junqi, W. Defang, L. Hui, H. Zuoli, Z. Zhenfeng, Appl. Surf. Sci. 257 (2011) 5879.
[15] X.F. Cheng, W.H. Leng, D.P. Liu, Y.M. Xu, J.Q. Zhang, C.N. Cao, J. Phys. Chem. C 112 (2008) 8725.
[16] D.A. Shirley, Phys. Rev. B 5 (1972) 4709.
[17] J.H. Scofield, J. Electron Spectrosc. Relat. Phenom. 8 (1976) 129.
[18] P. Kubelka, F. Munk, Z. Tech. Phys. 11a (1931) 593.
[19] V. Weidner, J. Hsia, J. Opt. Soc. Am. 71 (1981) 856.
[20] J. Rodriguez-Carvajal, Commission of Powder Diffraction, IUCr Newsletter 26 (2001) 12.
[21] J. Yu, Q. Xiang, J. Rana, S. Mann, Cryst. Eng. Commun. 12 (2010) 872.
[22] Q. Xiang, K. Lv, J. Yu, Appl. Catal. B: Environ. 96 (2010) 557.
[23] R. Dominko, L. Dupont, M. Gaberšček, J. Jamnik, E. Baudrin, J. Power Sources 174 (2007) 1172.
[24] G.L. Li, G.H. Wang, J.M. Hong, J. Mater. Sci. Lett. 18 (1999) 1243.
[25] Y. Huang, Y. Cao, G. Wang, V.C. Corberan, React. Kinet. Catal. Lett. 75 (2002) 31.
[26] M.G. Faba, D. Gonbeau, G. Pfister-Guillouzo, J. Electron Spectrosc. Relat. Phenom. 73 (1995) 65.
[27] J.C. Dupin, D. Gonbeau, P. Vinatier, A. Levasseur, Phys. Chem. Chem. Phys. 2 (2000) 1319.
[28] C. Guimon, A. Gervasini, A. Auroux., J. Phys. Chem. B 105 (2001) 10316.
[29] A.R. González-Elipe, G. Munuera, J.P. Espinos, J.M. Sanz, Surf. Sci. 220 (1989) 368.
[30] M.C. Biesinger, L.W.M. Lau, A. Gerson, R.St.C. Smart, Appl. Surf. Sci. 257 (2010) 887.
[31] J.C. Parlebas, M.A. Khan, T. Uozumi, K. Okada, A. Kotani, J. Electron Spectrosc. Relat. Phenom. 71 (1995) 117.
[32] J.L. Guimarãesa, M. Abbate, S.B. Betimb, M.C.M. Alves, J. Alloys Compd. 352 (2003) 16.
[33] D.K.G. de Boer, C. Haas, G.A. Sawatzky, Phys. Rev. B 29 (1984) 4401.
[34] I. Pollini, A. Mosser, J.C. Parlebas, Phys. Rep. 355 (2001) 1.
[35] A.E. Bocquet, T. Mizokawa, K. Morikawa, A. Fujimori, S.R. Barman, K. Maiti, D.D. Sarma, Y. Tokura, M. Onoda, Phys. Rev. B 53 (1996) 1161.
[36] Y. Xie, X. Zhao, Y. Li, Q. Zhao, X. Zhou, Q. Yuan, J. Solid State Chem. 181 (2008) 1936.
[37] J.C. Yu, J. Yu, W. Ho, Z. Jiang, L. Zhang, Chem. Mater. 14 (2002) 3808.
[38] D. Li, H. Haneda, S. Hishita, N. Ohashi, N.K. Labhsetwar, J. Fluorine Chem. 126 (2005) 69.
[39] R.D. Shannon, Acta Crystallogr. A 32 (1976) 751.
[40] K. Jirátová, J. Mikulová, J. Klempa, T. Grygar, Z. Bastl, F. Kovanda, Appl. Catal. A 361 (2009) 106.
[41] C.D. Wagner, W.M. Riggs, L.E. Davis, J.F. Moulder, G.E. Muilenberg (Eds.), Handbook of X-ray Photoelectron Spectroscopy, Perkin-Elmer, Eden Prairie, 1979.
[42] A.B. Murphy, Appl. Opt. 46 (2007) 3133.
[43] K.A. Michalow, D. Logvinovich, A. Weidenkaff, M. Amberg, G. Fortunato, A. Heel, T. Graule, M. Rekas, Catal. Today 144 (2009) 7.
[44] A.B. Murphy, Sol. Energy Mater. Sol. Cells 91 (2007) 1326.
[45] H. Tang, K. Prasad, R. Sanjines, P.E. Schmid, F. Levy, J. Appl. Phys. 75 (1994) 2042.
[46] K.M. Glassford, J.R. Chelikowsky, Phys. Rev. B 46 (1992) 1284.
[47] A. Mills, J. Wang, J. Photochem. Photobiol. A 127 (1999) 123.
[48] M. Ghaffari, P.Y. Tan, M.E. Oruc, O.K. Tan, M.S. Tse, M. Shannon, Catal. Today 161 (2011) 70.
[49] S. Liu, J. Yu, M. Jaroniec, J. Am. Chem. Soc. 132 (2010) 11914.
[50] A. Franco, M.C. Neves, M.M.L. Ribeiro Carrott, M.H. Mendonça, M.I. Pereira, O.C. Monteiro, J. Hazard. Mater. 161 (2009) 545.
[51] P.D. Kanhere, J. Zheng, Z. Chen, J. Phys. Chem. C 115 (2011) 11846.
[52] G. Li, G. Song, J. Chen, M. Zhu, P.K. Wong, in: 2nd Conference on Environmental Science and Information Application Technology, 2010.
[53] R.G. Nair, S. Paul, S.K. Samdarshi, Sol. Energy Mater. Sol. C 95 (2011) 1901.
[54] R. Asahi, T. Morikawa, T. Ohwaki, K. Aoki, Y. Taga, Science 293 (2001) 269.
[55] T. Ohno, T. Mitsui, M. Matsumura, Chem. Lett. 32 (2003) 364.
[56] Q. Xiang, J. Yu, M. Jaroniec, Phys. Chem. Chem. Phys. 13 (2011) 4853.
[57] J. Yu, G. Dai, B. Huang, J. Phys. Chem. C 113 (2009) 16394.
[58] N. Todorova, T. Giannakopoulou, T. Vaimakis, C. Trapalis, Mater. Sci. Eng. B-Adv. Funct. Solid-State Mater. 152 (2008) 50.
[59] N. Todorova, T. Giannakopoulou, G. Romanos, T. Vaimakis, Jiaguo Yu, C. Trapalis, Int. J. Photoenergy 2008 (2008) 1.
[60] T. Yamaki, T. Umebayashi, T. Sumita, S. Yamamoto, M. Maekawa, A. Kawasuso, H. Itoh, Nucl. Instrum. Methods Phys. Res. B 206 (2003) 254.
[61] D. Li, H. Haneda, N.K. Labhsetwar, S. Hishita, N. Ohashi, Chem. Phys. Lett. 401 (2005) 579.
[62] W. Ho, J.C. Yu, S. Lee, Chem. Commun. 10 (2006) 1115.
[63] K.M. Reddy, C.V.R. Gopal, S.V. Manorama, J. Solid State Chem. 158 (2001) 180.
[64] M. Radecka, K. Zakrzewska, M. Wierzbicka, A. Gorzkowska, S. Komornicki, Solid State Ionics 157 (2003) 379.
[65] R.B. Yahya, H. Hayashi, T. Nagase, T. Ebina, Y. Onodera, N. Saitoh, Chem. Mater. 13 (2001) 842.
[66] F. Amano, T. Yasumoto, T. Shibayama, S. Uchida, B. Ohtani, Appl. Catal. B 89 (2009) 583.
[67] V. Štengl, S. Bakardjieva, J. Šubrt, E. Večerníková, L. Szatmary, M. Klementová, V. Balek, Appl. Catal. B: Environ. 63 (2006) 20.
[68] L. Zhen, C.Y. Xu, W.S. Wang, C.S. Lao, Q. Kuang, Appl. Surf. Sci. 255 (2009) 4149.
[69] L.M. Torres-Martínez, I. Juárez-Ramírez, K.D. Ángel-Sánchez, L. Garza-Tovar, A. Cruz-López, G.D. Ángel, J. Sol–Gel Sci. Technol. 47 (2008) 158.
[70] B.L. Wang, Q. Chen, R.H. Wang, L.-M. Peng, Chem. Phys. Lett. 376 (2003) 726.